Combust. Sci. and Tech., 180: 2143–2169, 2008

ISSN: 0010-2202 print/1563-521X online
DOI: 10.1080/00102200802414915

A MODEL OF AP/HTPB COMPOSITE PROPELLANT COMBUSTION IN ROCKET-MOTOR ENVIRONMENTS

Weidong Cai, Piyush Thakre, and Vigor Yang
Department of Mechanical and Nuclear Engineering, The Pennsylvania State University, University Park, PA 16802

A comprehensive theoreticallnumerical model for treating AP/HTPB composite-propellant combustion in a rocket-motor environment is presented. The formulation takes into account the conservation equations in both the gas and condensed phases, and accommodates finite-rate chemical kinetics and variable thermophysical properties. The processes in the two phases are coupled at the surface to determine the propellant burning behavior. An asymptotic analysis based on a large activation-energy approximation for the condensed-phase decomposition is applied to help resolve the combustion wave structure in the interfacial layer. A simplified global reaction is employed to characterize the final diffusion flame between the decomposition products of AP and the pyrolysis products of HTPB. Only laminar flows are considered here, to avoid complications arising from turbulence. A detailed parametric study is conducted on the gas-phase flame structures of AP/HTPB composite propellants. The dependence of burning rate, flame stand-off distance, and heat-release distribution on AP particle size, chamber pressure, and gas-phase reaction rates is studied systematically. The phenomenon of erosive burning due to the strong crossflow in a rocket-motor environment is also examined.

Keywords: AP/HTPB composite propellant; Erosive burning; Solid rocket motor

INTRODUCTION

Ammonium perchlorate (AP)-based composite propellants have been a workhorse in the field of solid rocket propulsion for more than five decades. This type of propellant typically contains a multi-modal distribution of AP (NH_4ClO_4) grains ($\sim$20 to 200 μm) embedded in the hydroxyl-terminated polybutadiene (HTPB) matrix. The physical inhomogeneity of the propellant, along with a wide range of AP particle sizes, renders the combustion modeling a challenging task. The physiochemical processes that occur during the combustion of AP/HTPB propellant include condensed-phase heating, degradation of AP and HTPB, melting and surface pyrolysis, and gas-phase reactions. The flame structures and burning behavior depend on several factors, such as propellant composition, AP grain size, initial and ambient conditions, and propellant morphological configuration.

This work was sponsored partly by the Pennsylvania State University and partly by the California Institute of Technology Multidisciplinary University under ONR Grant No. N00014-95-1-1338, with Dr. Judah Goldwasser as the Program Manager.

Address correspondence to Vigor Yang, The Pennsylvania State University, 104 Research Building East, University Park, PA 16802, USA. E-mail: vigor@psu.edu

The combustion characteristics of AP-based composite propellants were extensively studied during the 1960s and 1970s under various rocket-motor development programs. Comprehensive reviews on the state of the knowledge up to the 1980s were written by Kishore (1979) and Ramohalli (1984). After a relative slump in research efforts in the following 15 years, there was a resurgence of interest in AP-based propellants on account of the progress in experimental diagnostics and numerical simulations. An overview of recent advances in AP/HTPB propellant pyrolysis and combustion from an experimental perspective is provided by Brill and Budenz (2000).

Early combustion modeling efforts focused on correlating measured burning rates under stagnant conditions. Some of the well-known examples are the 'sandwich columnar diffusion flame' model by Nachbar and Parks (1960), the "granular diffusion flame" model by Summerfield et al. (1960), the "thermal layer theory" by Chaiken and Anderson (1960), and the "petite ensemble" model based on a statistical approach by Glick (1974). These models are predominantly based on gas-phase processes, with condensed-phase processes either neglected or treated in a rudimentary fashion. In contrast, some researchers regarded condensed-phase decomposition as the most important factor (Hermance, 1960; Waesche, 1969). A significant improvement in predicting the propellant burning rates was achieved by Beckstead et al. (1970) by incorporating a multi-flame structure in the gas phase. Three separate flames were identified in the gas phase: 1) primary premixed oxidizer flame (i.e., the AP deflagration wave), 2) primary diffusion flame between the decomposition products of the binder and oxidizer, and 3) final diffusion flame between the products of the above two flames. A more detailed description of the combustion-zone microstructure was provided by Price et al. (1986), recognizing the presence of the leading-edge flame (LEF). It was observed that the diffusion flame cannot extend all the way to the propellant surface, due to the low temperature in that region.

As interest in the modeling of composite-propellant combustion was rekindled in the mid 1990s, several two-dimensional models were developed to address various fundamental issues. The most prominent among them were proposed by Jia and Bilger (1994), Buckmaster et al. (1999), Knott and Brewster (2000), and Ramakrishna et al. (2002). In addition, measurements were conducted by Price (1995), Parr and Hanson-Parr (1996), and Chorpening and Brewster (2002) on two-dimensional sandwich propellant combustion, to provide data for model validation. The sandwich geometry has long been recognized in most modeling studies as a useful framework for investigating combustion mechanisms associated with composite propellants.

Jia and Bilger (1994), in their two-dimensional analytical model of AP/HTPB sandwich propellant combustion, emphasized the importance of a finite Peclet number (*Pe*) due to the prevalence of both diffusive and convective transport. One of their important findings was that the stoichiometric contour at a finite *Pe* does not necessarily intersect the propellant surface at the fuel-oxidizer interface. The work was later extended to allow treatments of heterogeneous, multi-modal propellant combustion for non-planar surface geometries (Bilger et al., 1996). Buckmaster et al. (1999) made additional contributions by investigating the effects of propellant geometry/stoichiometry on flame structure for a finite *Pe* by employing finite-rate gas-phase chemistry. Results indicate that the flame occupies only a portion of the stoichiometric contour with the presence of leading-edge flames.

Knott and Brewster (2000) adopted a similar approach, but included the coupling between the gas- and condensed-phase processes. A two-step chemical kinetics mechanism was employed, consisting of a high activation-energy condensed-phase decomposition reaction and a low activation-energy gas-phase reaction. A linearized reaction-rate expression was assumed to obtain analytical solutions. The analysis was further developed to formulate a numerical model for studying the flame structure and surface topology of two-dimensional non-planar AP/HTPB laminate propellants with different AP particle sizes (Knott and Brewster, 2002). Good agreement was achieved with the experimental observations in terms of the protrusion/recession of oxidizer and binder, an important feature of the burning surface topography. Hegab et al. (2001) improved the model by Buckmaster et al. (1999) by including the thermal field in the condensed phase with appropriate jump conditions across the gas-solid interface. A simple Arrhenius pyrolysis law was used to obtain the local burning rate. The propagation of the nonplanar burning surface was described by means of a level-set formulation. Ramakrishna et al. (2002) established a numerical model by considering two-dimensional features in both the gas and condensed phases. A three-step kinetics model was adopted to capture the distributed flame structure. In addition to the burning-rate calculations, the model reasonably predicts the low-pressure deflagration limit of AP/HTPB sandwich propellants.

Recently, efforts have been made by Knott et al. (2001), Jackson and Buckmaster (2002), and Massa et al. (2005) to evolve the AP/HTPB propellant combustion modeling from a simplified two-dimensional sandwich-type of geometry to a more realistic configuration with complex particle packing. The effects of particle-size distribution and surface topology on the burning behavior of propellants were systematically investigated. The gas-phase kinetics initially treated with a two-step kinetics scheme (Jackson and Buckmaster, 2002) was improved to a three-step mechanism (Massa et al., 2005).

The models discussed so far do not take into account the effect of crossflows encountered in practical rocket-motor environments. It is well established that the propellant burning rate depends on the crossflow velocity, through its influence on the local transport processes near the propellant surface. This phenomenon, commonly referred to as erosive burning, may substantially affect the propulsive performance and reliability of a rocket motor. King (1978) developed a model of erosive burning for composite-propellant combustion based on the crossflow-induced flame bending phenomenon. The burning rate, however, was over-predicted for low crossflows and under-predicted for high crossflows. The model was later improved by considering turbulence-enhanced transport in addition to the flame bending (King, 1981). The treatment was empirical in nature.

Beddini (1978) and Razdan and Kuo (1982) attributed the increase of the burning rate in a crossflow to turbulence effects, and modeled this phenomenon by means of a second- and a first-order closure scheme, respectively. The former approach is highly idealized and not representative of the typical flame structures for composite propellants. The latter assumed diffusion-controlled reaction rates in the gas phase and neglected the multi-flame structure inherent in the combustion of composite propellants. Moreover, the gas-phase heat release is totally controlled by the eddy breakup. This renders the approach unsuitable for low-speed laminar flows, where the crossflow-induced turbulence is negligible but erosive burning is still

observed. Tseng and Yang (1994) noted, in their numerical study of homogenous solid-propellant combustion in rocket-motor environments, that the burning-rate enhancement occurs when turbulence penetrates down to the flame zone above the propellant surface and increases the local heat-transfer rate to the condensed phase. Renie and Osborn (1983) and Godon et al. (1992) also developed models to predict erosive burning, with an approach similar to King's model (1981), particularly in the treatment of the fluid dynamics.

The present work attempts to develop a comprehensive theoretical/numerical model for treating AP/HTPB composite-propellant combustion in a rocket-motor environment. The analysis is based on the complete conservation equations in both the gas and condensed phases, and accommodates finite-rate chemical kinetics and variable thermophysical properties. An asymptotic analysis employing the large activation-energy approximation is applied to describe the condensed-phase decomposition in the interfacial layer. The gas- and condensed-phase processes are matched at the interface to determine the propellant burning behavior. Only laminar flows are considered here, to avoid complications arising from turbulence. A detailed parametric study is conducted on the gas-phase flame structure. The dependence of burning rate, flame stand-off distance, and heat-release distribution on AP particle size, chamber pressure, and gas-phase reaction rates is studied systematically.

COMBUSTION MODEL FOR AP/HTPB COMPOSITE PROPELLANT

The combustion of AP/HTPB composite propellant involves an array of intricate physiochemical processes including: (1) conductive preheating, decomposition, and phase transition in the condensed phase; and (2) multi-stage reactions in the gas phase. Since the oxidizer and fuel binder are not linked chemically, the combustion characteristics of AP and HTPB are first examined separately in order to facilitate the construction of an integrated model for the overall propellant combustion.

Combustion of AP Monopropellant

AP monopropellant combustion has been studied extensively in the past (Guirao and Williams, 1971). The AP crystal first experiences a phase transition from an orthorhombic structure to a cubic structure at 513 K. As the temperature increases, the crystal lattice becomes unstable and melts around 830 K. Equilibrium dissociative sublimation and degradation of AP occurs at this temperature. The degradation results in a thin superficial reaction layer, accounting for 70% consumption of the AP crystal. The remaining 30% undergoes a highly endothermic equilibrium dissociative sublimation ($\Delta H_{dis} = 58 \pm 2.$ kcal/mol) through a proton transfer producing gaseous ammonium and perchlorate acid. The species so generated subsequently undergo a sequence of chain reactions to form a premixed flame producing final products such as O_2, NO, and N_2O, which act as major oxidizers in the gas-phase reactions.

Based on the experimental work of Jacobs and Whitehead (1969), Guirao and Williams (1971) established a gas-phase reaction mechanism involving 14 species and 10 reactions to predict the temperature field and species concentrations. Following this mechanism, Chu and Yang (1996) employed a one-step kinetics model and

successfully predicted the flame temperature and major species concentrations of AP deflagration. Results indicate that the premixed flame is located very close to the propellant surface, with stand-off distances of about 9 and 1 μm at pressures of 20 and 70 atm, respectively. Figure 1 shows a schematic of the physicochemical processes described above. The flame height of AP monopropellant is about 1 to 2 orders of magnitude lower than that of the final diffusion flame in AP/HTPB composite propellant combustion. As a first attempt, the AP deflagration in the gas phase is assumed to be a surface phenomenon, which takes place simultaneously with the condensed-phase decomposition. Thus, in the present model, the condensed phase includes a preheated zone and a superficial reaction layer (which includes the melt layer and the AP deflagration zone). A one-step reaction model (R1) is employed, based on the work of Guirao and Williams (1971).

$$\mathrm{AP} \rightarrow 1.62\ \mathrm{H_2O} + 1.105\ \mathrm{O_2} + 0.265\ \mathrm{N_2} + 0.12\ \mathrm{N_2O} + 0.23\ \mathrm{NO} + 0.76\ \mathrm{HCl} + 0.12\ \mathrm{Cl_2} \qquad \text{(R1)}$$

Pyrolysis of HTPB Binder

HTPB is long-chain, cross-linked, and high molecular-weight polymer. Beck (1987) pointed out that the pyrolysis of HTPB is highly dependent on the heating rate. At low heating rates (less than 100 K/min), the pyrolysis is known to occur via a two-stage mechanism. The first stage involves endothermic depolymerization, forming monomer butadiene, cyclopentene, 1,3-cyclohexadiene, and 4-vinylcyclohexene as the main gaseous products. Thermogravimetric analysis (TGA) studies show a 10–15% weight loss during this stage. In the second stage, the remaining residue cyclyzes, cross-links, and undergoes further degradation. At heating rates higher than 100 K/min, the first stage prevails, with deploymerization as the main degradation process (Chen and Brill, 1991; Arisawa and Brill, 1996). In rocket-motor environments, since HTPB is exposed to extreme temperatures (above 2000 K), pressures (20–100 atm), and heating rates (as high as 10^6 K/s), there is very little time for exothermic cross linking and cyclization to take place.

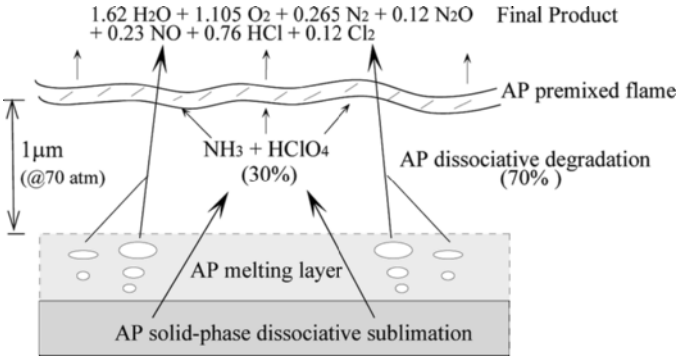

Figure 1 Combustion wave structure of AP monopropellant.

Consequently, depolymerization becomes the dominant process. Radhakrishnan and Rama Rao (1981) identified the final degradation products using a gas chromatography (GC) technique. At temperatures below 770 K, the main gaseous product is butadiene, whereas a whole range of products arises as the temperature increases. At 1170 K, butadiene accounts for only 1–2% of the products, and the primary product is ethylene. In light of the above findings, the thermal decomposition of HTPB in a rocket-motor environment is assumed to undergo the following pathway:

$$\text{HTPB} \rightarrow C_2H_4 \text{ and light hydrocarbon species} \qquad \text{(R2)}$$

Combustion of AP/HTPB Propellant

Three facts are realized for a typical AP/HTPB composite propellant under consideration. First, the mass loading of AP is much higher than that of HTPB. Second, AP monopropellant is highly reactive and can sustain exothermic reactions without the presence of any fuel binder. Third, the size of AP particles plays a decisive role in dictating the burning behavior of the composite propellant. AP degradation is thus regarded as the controlling factor in the modeling of condensed-phase processes. HTPB is assumed to influence the combustion only through the participation of its degradation products in the gas-phase reactions. Consequently, the condensed-phase modeling is conducted solely on AP, and the HTPB regression rate is determined by the overall energy balance. A primary diffusion flame can occur through the reactions between HTPB pyrolysis products and ammonia-derived oxidizer ($HClO_4$). This flame, however, may exist only at low pressures, due to the competing reaction effects. In rocket motors, the high chamber pressure renders rapid AP deflagration with an exceedingly low flame height. The ammonia-derived oxidizer can hardly meet HTPB pyrolysis species through the diffusion process, and is almost completely consumed in the AP primary flame. The effect of the primary diffusion flame can thus be neglected in a high-pressure environment.

To facilitate modeling, the overall pyrolysis product of HTPB is assumed to be ethylene. The validity of this approach is further corroborated by the chemical equilibrium analyses of AP/HTPB and AP/ethylene (Gordon and McBride, 1994).

Table 1 Comparison of AP/HTPB and AP/C_2H_4 combustion under equilibrium conditions at 70 atm and a mass fraction of 80/20

	AP/HTPB	AP/C_2H_4
Adiabatic flame temperature (K)	2322.3	2403.5
Mole Fraction		
CO	.26995	.25615
CO_2	.04621	.03474
Cl	.00048	.00067
H	.00105	.00185
HCl	.14745	.13825
H_2	.22737	.26879
H_2O	.23329	.22970
NH_3	.00002	.00003
N_2	.07395	.06944
OH	.00021	.00034

Table 1 summarizes the adiabatic flame temperature and species concentrations of the two cases at an initial temperature of 300 K and pressure of 70 atm. The mass fraction of AP is 80% for both cases. Fairly good agreement is obtained for the equilibrium species concentration. The flame temperature, however, is over predicted by 100 K if HTPB is replaced by C_2H_4, a phenomenon attributed to the endothermic depolymerization and pyrolysis of HTPB to form C_2H_4. Figure 2 shows the effects of AP mass fraction on the adiabatic flame temperature and CO concentration for AP/HTPB and AP/ethylene mixtures. The results compare well and both mixtures exhibit the highest flame temperature when the AP mass fraction reaches a stoichiometric value of 88%. The substitution of ethylene for the HTPB pyrolysis products in the current modeling of the gas-phase combustion appears to be reasonable. Figure 3 illustrates the entire combustion wave structure considered in the present model.

The overall gas-phase reaction can be expressed as

$$4.27\ \mathrm{Ox} + 0.523\ \mathrm{C_2H_4} \rightarrow 5.257\ \mathrm{Pr} \qquad \text{(R3)}$$

where Ox stands for the oxidizing species from AP deflagration, having the following composition

$$4.27\mathrm{Ox} = (1.62\mathrm{H_2O} + 1.105\mathrm{O_2} + 0.262\mathrm{N_2} + 0.12\mathrm{N_2O} + 0.23\mathrm{NO} + 0.76\mathrm{HCL} + 0.12\mathrm{Cl_2})$$

The products Pr from the final diffusion flame are

$$5.257\mathrm{Pr} = (0.4686\mathrm{CO} + 0.5773\mathrm{CO_2} + 0.0931\mathrm{Cl} + 0.0378\mathrm{H} + 0.8708\mathrm{HCl} + 0.2364\mathrm{H_2} + 2.269\mathrm{H_2O} + 0.477\mathrm{N_2} + 0.0288\mathrm{NO} + 0.0133\mathrm{O} + 0.1391\mathrm{OH} + 0.0499\mathrm{O_2})$$

In the above reaction (R3), the mass fraction of AP is selected to be the stoichiometric value of 88% for the AP/HTPB composite propellant. The composition of

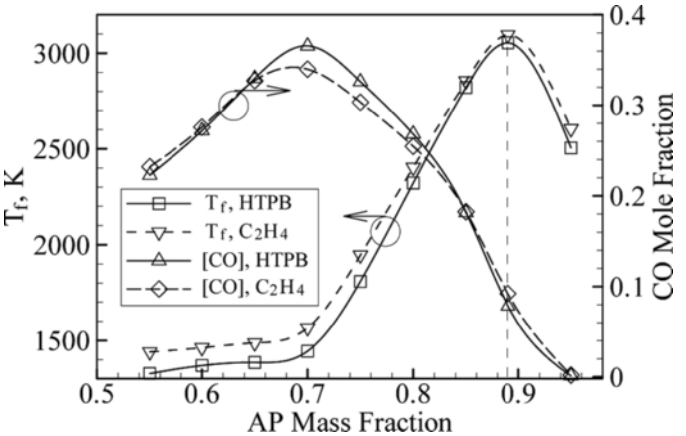

Figure 2 Adiabatic flame temperature and CO concentration of AP/HTPB and AP/C_2H_4 combustion under equilibrium condition, $p = 70$ atm and $T_i = 300$ K.

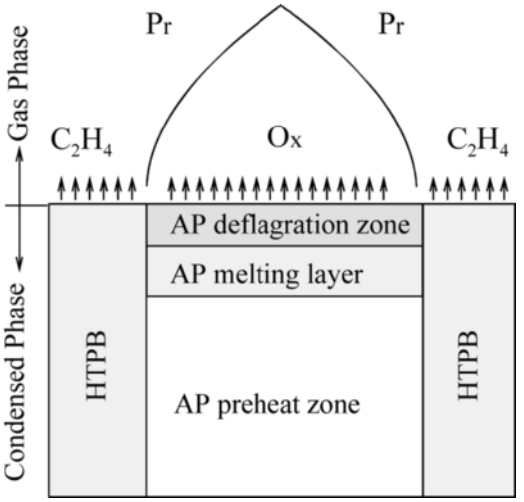

Figure 3 Schematic diagram of AP/HTPB combustion wave structure.

the product species is obtained from the chemical equilibrium calculations (Gordon and McBride, 1994).

THEORETICAL FORMULATION

The physical model considered in the present study is shown schematically in Figure 4. It consists of a cylindrical chamber loaded with AP/HTPB composite propellant and an exhaust nozzle. A sandwich-type of segment containing AP and HTPB is embedded in the propellant grain. The location of the sandwich in the motor can be varied, such that the burning properties and combustion wave structures of the propellant can be studied in different flow environments.

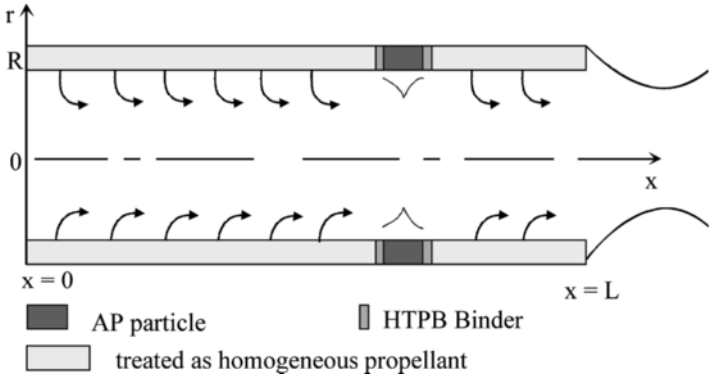

Figure 4 Schematic diagram of rocket motor loaded with AP/HTPB propellant.

Gas Phase

The gas-phase processes can be described by conservation equations of mass, momentum, energy, and species concentrations in axisymmetric coordinates, written in the following vector form

$$\frac{\partial \mathbf{Q}}{\partial t} + \frac{\partial}{\partial x}(\mathbf{E} - \mathbf{E_v}) + \frac{\partial}{\partial y}(\mathbf{F} - \mathbf{F_v}) = \mathbf{S} \tag{1}$$

where x and y denote the axial and radial coordinates, respectively. The variable vector $\mathbf{Q}$ is defined below.

$$\mathbf{Q} = y^{\delta}\,[\rho, \rho u, \rho v, \rho e, \rho\, Y_i]^T \tag{2}$$

where $\delta = 1$ and 0, respectively, for axisymmetric and two-dimensional flows. The details of the gas-phase formulation, including the explicit expressions for the convective flux vectors, $\mathbf{E}$ and $\mathbf{F}$, the diffusive flux vectors, $\mathbf{E_v}$ and $\mathbf{F_v}$, and the source vector, $\mathbf{S}$ can be found in Cai (2001) and Roh et al. (1995). Within the thermodynamic regime of concern, the specific heat C_P, viscosity μ, and thermal conductivity λ of each species are approximated by fourth-order polynomials of temperature. For mixtures, C_P is calculated by mass-averaging, and μ and λ by using Wilke's mixing rule (Reid et al., 1987). The binary mass diffusivity D_{ij} between species i and j is obtained by means of the Chapman-Enskog theory in conjunction with the Lennard-Jones intermolecular potential energy function (Reid et al., 1987). The effective diffusion coefficient D_{im} for a multi-component mixture is calculated using the binary diffusion coefficients (Tseng and Yang 1994; Cai, 2001).

Chemical Kinetics

A zeroth-order reaction (R1) is assumed for the decomposition of AP. The rate of mass production of AP is given as

$$\dot{\omega}_{AP} = -Ap^n \exp(-E_{AP}/R_u T) \tag{3}$$

where the activation energy, E_{AP}, is taken as 22 kcal/mol and the reaction order, n, as 1.8 (Beckstead, 1970). The pre-exponential factor, A, is calibrated as 7×10^4 $\mathrm{Pa}^{-1.8}$ from the experimental data at $p = 40$ atm (Seleznev et al., 1969). The one-step global reaction model of Westbrook and Dryer (1981) is employed to treat the reaction (R3) between C_2H_4 and the oxidizer species. The effects of all the oxidizing species are taken into account by considering the oxygen content in each species. The rates of mass production are:

$$\dot{\omega}_{C_2H_4} = -A \exp(-E_a/R_u T)\rho^{1.75}\, Y_{C_2H_4}^{0.1}\, Y_{Ox}^{1.65}\, (WM_{C_2H_4}^{0.9}/WM_{Ox}^{1.65}) \tag{4}$$

$$\dot{\omega}_{Ox} = 8.09\, \dot{\omega}_{C_2H_4} \tag{5}$$

where the activation energy, E_a, is 30 kcal/mol, and the pre-exponential factor, A, is $2.0 \times 10^{12}(\mathrm{m}^3/\mathrm{kgmole})^{0.75}\mathrm{s}^{-1}$. Direct application of the chemical kinetics in Eq. (4)

to a preconditioned semi-implicit numerical scheme causes several difficulties in computing the associated Jacobian matrices. To circumvent this problem, the exponents of the fuel and oxidizer mass fractions are set to unity. The pre-exponential factor is recalibrated to retain the same reaction rate as predicted by Westbrook and Dryer's model (1981) over the range of fuel and oxidizer mass fractions of concern. The pre-exponential factor used in the present analysis has the value of 1.09×10^9 $(\mathrm{m}^3/\mathrm{kmol})^{0.75}$, whereas the activation energy remains unchanged.

AP Deflagration

The AP condensed phase consists of a preheated zone and a thin superficial reaction layer, in which thermal diffusion and decomposition reactions take place. With the neglect of mass diffusion and axial heat transfer, the governing equations for the condensed-phase process reduce to

$$\text{Mass: } \dot{m}_{AP} = \rho_{AP} r_b \tag{6}$$

$$\text{Energy: } \bar{\rho}_{AP} C_{AP} \frac{\partial T}{\partial t} + \dot{m}_{AP} \overline{C}_{AP} \frac{\partial T}{\partial y} = \frac{\partial}{\partial y}\left(\bar{\lambda}_{AP} \frac{\partial T}{\partial y}\right) + Q_{AP} \dot{\omega}_{AP} \tag{7}$$

$$\text{Species: } \bar{\rho}_{AP} \frac{\partial Y_{AP}}{\partial t} + \dot{m}_{AP} \frac{\partial Y_{AP}}{\partial y} = \dot{\omega}_{AP} \tag{8}$$

where $\bar{\rho}_{AP}, \overline{C}_{AP},$ and $\bar{\lambda}_{AP}$ denote the mass-averaged density, specific heat, and thermal conductivity of AP and AP-derived decomposition products, respectively, and r_b the propellant burning rate. The volumetric heat release from the condensed-phase reaction, Q_{AP}, is determined by the difference between the heats of formation of AP and its decomposition products. The in-depth boundary conditions associated with Eqs. (7) and (8) are $T = T_i$ and $Y_{AP} = 1$, at $y = -\infty$, respectively, where T_i is the preconditioned propellant temperature. At the end of the primary AP monopropellant flame, a complete decomposition of AP occurs, with $Y_{AP} = 0$ and $T = T_s$.

To solve for the eigenvalue $\dot{m}_{AP}$ for the condensed-phase process, an additional equation is required. Following the approach of Lengelle (1970) and Ibiricu and Williams (1975), a matched asymptotic expansion analysis based on the large activation-energy approximation is applied to the reaction layer. The resultant burning-rate formula (Cai, 2001) is expressed as

$$r_b^2 = \alpha_{AP}\left(\frac{A p^n e^{-\beta}}{\beta}\right) \frac{1}{\dfrac{\lambda_g}{\dot{m}_{AP} C_{AP} T_s}\left(\dfrac{\partial T}{\partial y}\right)_s + \dfrac{Q_{AP}}{2 C_{AP} T_s}} \frac{Q_{AP}}{Q_s(T_s)} \tag{9}$$

where

$$Q_s(T_s) = C_{AP} T_s + \Delta h^0_{f,AP} - C_{\mathrm{Ox}} T_s - \Delta h^0_{f,\mathrm{Ox}} \tag{10}$$

and $\beta (\equiv E_{AP}/R_u T_s)$ is the nondimensional activation energy for the condensed-phase thermal decomposition. Equation (9) shows the dependence of the propellant

burning rate on the chamber pressure and heat feedback from the gas-phase flame zone to the propellant surface, as well as the heat release in the condensed phase.

The recession rates of the AP and HTPB surfaces are linked by assuming that the mass consumption rate of each ingredient is proportional to its original mass ratio. The energy needed for the HTPB pyrolysis comes from two sources: exothermic decomposition of AP and the heat feedback from the gas-phase flame. If the latter prevails, then the required energy is provided solely from the gas-phase flame. Otherwise, the energy is compensated by the heat release from the AP decomposition and deflagration. In this case, the heat release term Q_{AP} in Eq. (9) is replaced by $Q_{AP} - Q_{AP\rightarrow HTPB}$, where $Q_{AP\rightarrow HTPB}$ is the energy provided from the AP decomposition to support the HTPB pyrolysis. The HTPB condensed-phase process is characterized by the following global mass and energy conservation equations.

$$\dot{m}_{HTPB} = \rho_{HTPB} r_b \tag{11}$$

$$\dot{m}_{HTPB}[C_{HTPB}(T_s - T_i) + \dot{Q}_{HTPB}] = \lambda \left.\frac{\partial T}{\partial y}\right|_g + \dot{Q}_{AP\rightarrow HTPB} \tag{12}$$

NUMERICAL METHOD

The rocket-motor internal flowfield typically features a low Mach-number regime, for which the conservation equations are poorly coupled. The resultant disparity in the system eigenvalues degrades the numerical convergence rate significantly. The stiff source terms arising from chemical reactions pose another severe challenge. The time and length scales associated with chemical processes are much smaller than their counterparts for the flow transients. An explicit numerical algorithm is an inefficient way of treating the temporal integration, because a very small time-step is required to ensure numerical stability. A fully implicit method is not suitable for multi-dimensional flow problems either, due to the requirement of prohibitively large computing resources.

To circumvent these difficulties, a preconditioning technique with dual-time stepping integration is employed (Tseng and Yang, 1994; Hsieh and Yang, 1997; Zong and Yang, 2007). The system eigenvalues are rescaled to the same order of magnitude, thereby improving substantially the numerical convergence rate. A semi-implicit four-step Runge-Kutta scheme is implemented to resolve the numerical stiffness issue. The source terms are split into two parts: those associated with chemical reactions and otherwise. The former are treated implicitly and the later explicitly. Since the chemical source terms can be easily separated from the rest of the equations, this method is more efficient than a fully explicit scheme and requires much less computational resources. The semi-implicit scheme is also suitable for parallel processing. The spatial discretization scheme is achieved with a second-order central difference scheme. In order to capture the steep gradients of temperature and species concentrations in the flame zone, matrix dissipation incorporated with a total-variation-diminishing (TVD) switch is implemented (Oefelein, 1997; Shuen et al., 1990).

RESULTS AND DISCUSSION

AP Monopropellant Combustion

Table 2 lists the thermophysical properties of AP and HTPB. The AP monopropellant combustion is first studied using the analytical model developed above. Figures 5 and 6, respectively, show the distributions of temperature and AP species concentration at two different pressures of 40 and 100 atm under adiabatic conditions. The corresponding flame thickness is about 3.2 and 1.2 μm, respectively. The reaction is initiated around the same location but extends over a shorter distance for a higher pressure. Figure 7 shows the pressure sensitivity of the burning rate and the adiabatic flame temperature. Good agreement is obtained with experimental data of Seleznev (1969), suggesting the capability of the present model in capturing the main features of AP monopropellant combustion. The calculated adiabatic flame temperature is slightly lower than the value predicted by the chemical equilibrium analysis (Gordon and McBride, 1994). The maximum error of 4% could be attributed to the use of constant thermophysical properties in the model.

Motor Internal Flowfield and Baseline AP/HTPB Flame Structure

Figure 4 shows the physical domain, which consists of an axisymmetic chamber with a closed head-end, measuring 0.12 meter in length and 1 cm in diameter. Only the upper half of the volume is treated because of the flow symmetry with respect to the centerline. To begin with, the AP/HTPB propellant segment is located 6.5 mm downstream of the head-end in order to minimize the influence of crossflow on the propellant combustion. The AP oxidizer is 200 μm in width (d_{AP}). The HTPB segment size (d_{HTPB}) is determined by the following expression to ensure that the recession rate matches that of the AP.

$$\frac{d_{AP}}{d_{HTPB}} = \alpha \frac{\rho_{HTPB}}{\rho_{AP}} \tag{13}$$

where α is the mass ratio of AP to HTPB in the propellant. In the present study, $d_{AP} = 200\,\mu\text{m}$ and α has a typical value of 7/3 for practical motor propellants. The width of the HTPB element (d_{HTPB}) is thus set to 171 μm. Inert gases simulating the combustion products from the propellant are injected from the rest of the wall

Table 2 Thermophysical properties of AP and HTPB

Parameter	Value
ρ_{AP}	$1900\,\text{kg/m}^3$
ρ_{HTPB}	$950\,\text{kg/m}^3$
λ_{AP}	0.402 W/m.K
C_{AP}	1460 J/kg.K
C_{HTPB}	2860 J/kg.K
Q_{AP}	-1.23×10^6 J/kg

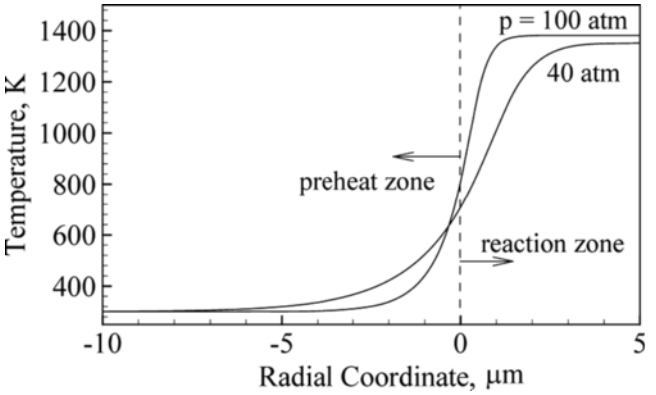

Figure 5 Temperature distributions of AP monopropellant combustion at 40 and 100 atm.

at a prescribed chamber pressure. The influx of the injected gases is determined as follows.

$$\dot{m}_{inert} = \frac{\dot{m}_{AP} \cdot d_{AP} + \dot{m}_{HTPB} \cdot d_{HTPB}}{d_{AP} + d_{HTPB}} \tag{14}$$

where $\dot{m}_{AP}$ and $\dot{m}_{HTPB}$ are the AP and HTPB mass fluxes from the sandwich segment, obtained from the matching between the gas- and condensed-phase processes.

The motor internal flow field is examined first. Figure 8 shows the distributions of two velocity components and the gauge pressure, which is defined as the difference from the mean pressure of 100 atm. The pressure field is nearly one-dimensional throughout the chamber, except in the combustion region where large density and temperature variations occur. The entire flow distribtuion bears a close resemblance to that in a chamber with surface transpiration (Apte and Yang, 2001). Figure 9 shows contour plots of the mass fractions of fuel, oxidizer, and product species. The diffusion flame tends to close over the oxidizer, forming an over-ventilated flame

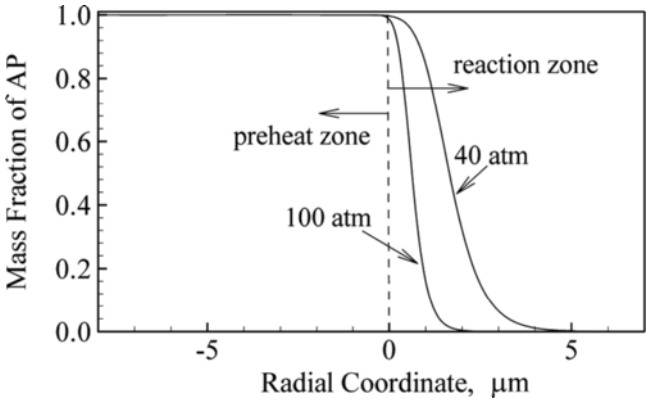

Figure 6 Distributions of AP mass fraction at 40 and 100 atm.

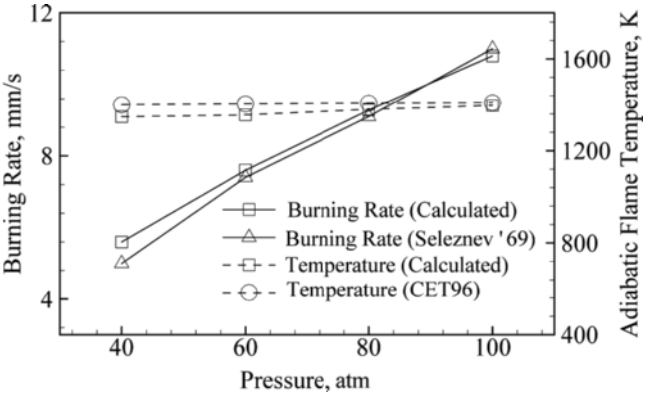

Figure 7 Pressure dependence of burning rate and adiabatic flame temperature of AP monopropellant combustion.

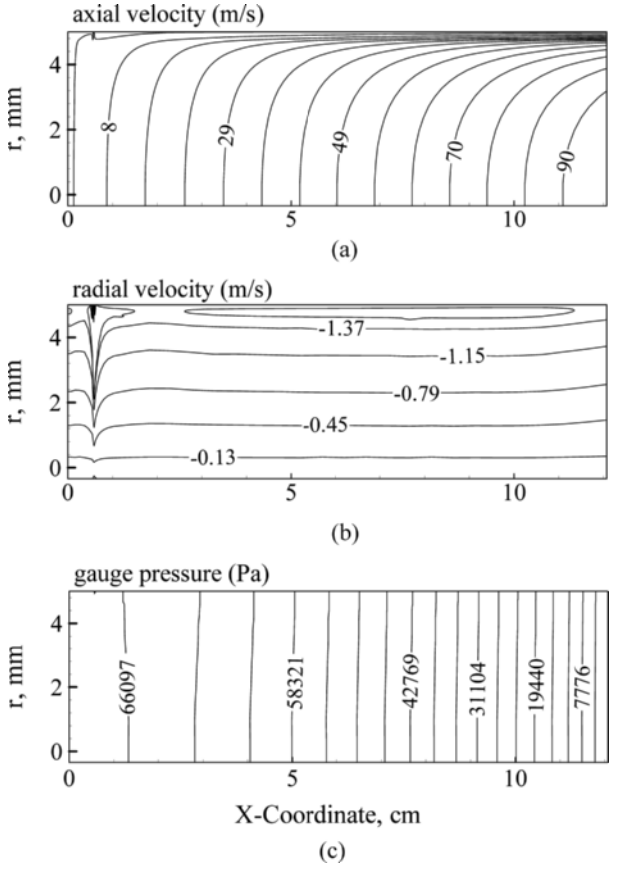

Figure 8 Contour plots of velocity and pressure ($p = 100$ atm, AP/HTPB: 70/30 and $d_{AP} = 200\,\mu$m).

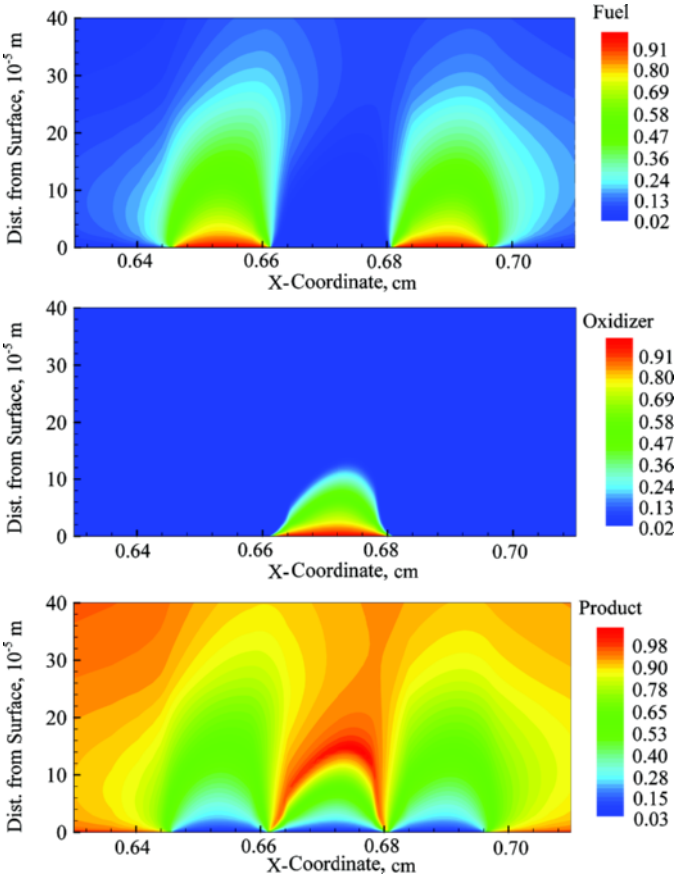

Figure 9 Distributions of mass fractions of fuel, oxidizer, and product at $p = 100$ atm (AP/HTPB: 70/30 and $d_{AP} = 200\,\mu$m).

due to the fuel-rich nature of the radial flow. As expected, the concentrations of the product species exhibit high values at the location of the final diffusion flame. The temperature distribution shown in Figure 10 indicates a flame height of about 140 μm.

The maximum temperature of 3400 K in the flame zone is 200 K higher than the value obtained from the equilibrium analysis for AP/ethylene. This discrepancy may arise from the use of a fixed AP mass fraction of 88% in calibrating the stoichiometric coefficients in the overall gas-phase reaction (R3). In reality, the flame may experience a range of oxidizer mass fractions in a convective flow environment. Figure 11 shows the heat-release distribution, exhibiting a nearly symmetric flame structure due to the weak crossflow near the chamber head-end. Figure 12 shows the pressure field and streamlines in the flame region. The pressure gradients due to strong heat release push the incoming gases from the upstream region away from the flame zone, causing a reversal of the local flow. The radial velocity increases nominally across the flame due to the volume dilation effect.

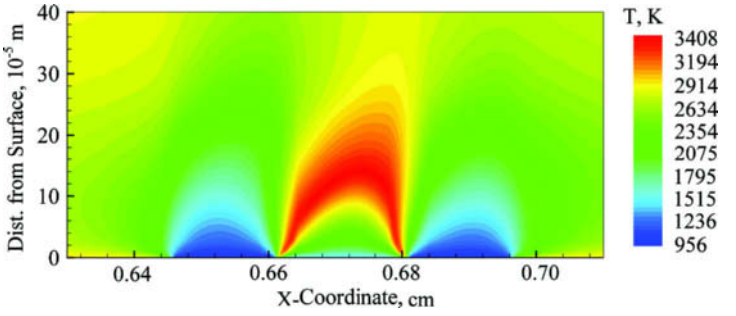

Figure 10 Temperature distribution at $p = 100$ atm (AP/HTPB: 70/30 and $d_{AP} = 200\,\mu$m).

Figure 13 shows the distributions of species concentrations at 1 μm above the propellant surface. The high reactivity of the fuel and oxidizer species leads to an extremely thin flame. Figure 14 shows the corresponding distributions of temperature and heat-release rate. As indicated in Figure 12, the local flow expansion in the flame zone may lead to a reversal of the incoming stream. The situation holds true especially in the upstream region of the motion, where the convective flow velocity is low. This phenomenon is substantiated in the velocity and pressure disturbances shown in Figure 15. The adverse pressure gradient at the left (upstream) edge of the flame causes a rapid decrease in the axial velocity. In contrast, the gases at the right (downstream) edge are pushed farther downstream due to a favorable pressure gradient and volume expansion across the flame. Such large variations of the velocities result in strong vortices around the flame.

Parametric Study on AP/HTPB Combustion

The burning behavior and flame structure of an AP/HTPB composite propellant are influenced by many factors including the chamber pressure, local velocity, and AP particle size and mass fraction. A parametric study was performed to investigate the effect of these factors on the propellant combustion characteristics. To facilitate discussion, three time scales are introduced, namely, diffusion time t_d,

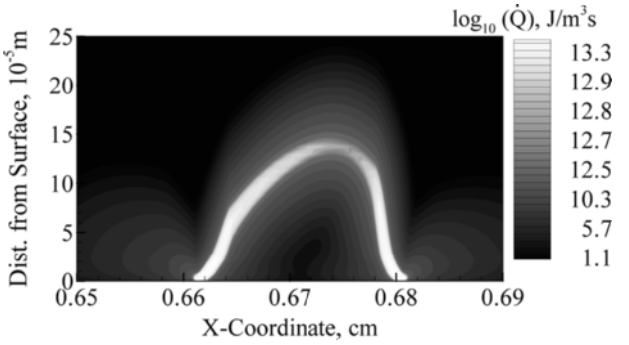

Figure 11 Distribution of heat-release rate at $p = 100$ atm (AP/HTPB: 70/30 and $d_{AP} = 200\,\mu$m).

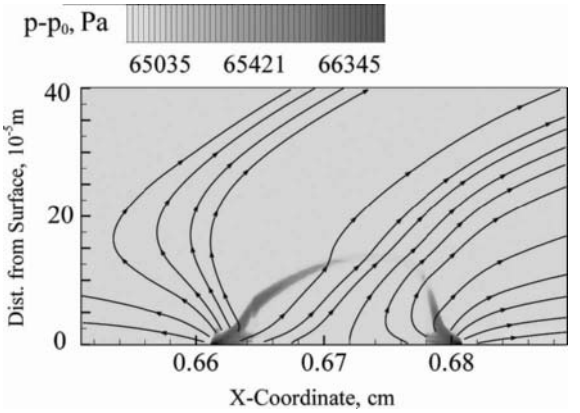

Figure 12 Streamlines and pressure field in near field of AP/HTPB flame zone ($p = 100$ atm, AP/HTPB: 70/30 and $d_{AP} = 200\,\mu$m).

radial flow residence time t_F, and reaction time t_c. They are estimated, respectively, by the following expressions.

$$t_d = d^2/D;\ \ t_F = \delta_f \rho/\dot{m}_{AP};\ \ t_c = \rho/\dot{\omega} \tag{15}$$

where d is the oxidizer diameter, δ_f the diffusion flame height, D the effective mass diffusivity, and $\dot{\omega}$ the mass production rate. Furthermore, two non-dimensional parameters (Peclet Pe and Damköhler Da numbers) characterizing the relative magnitudes of the above time scales are defined as follows:

$$Pe = t_d/t_F = \dot{m}_{AP} d^2/\rho D Z_f \tag{16}$$

$$Da = t_d/t_c = d^2\dot{\omega}/\rho D \tag{17}$$

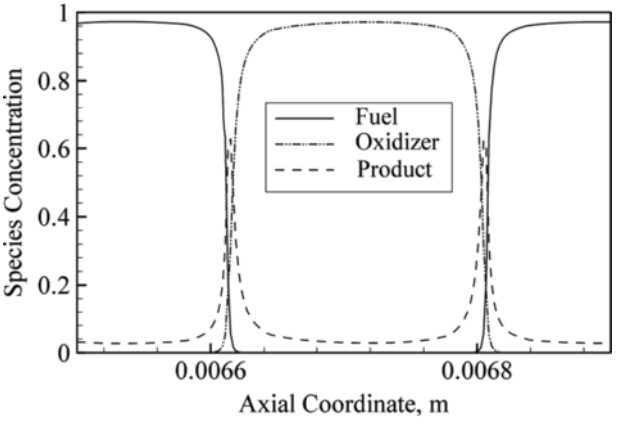

Figure 13 Species-concentration distributions at 1 μm above propellant surface ($p = 100$ atm, AP/HTPB: 70/30 and $d_{AP} = 200\,\mu$m).

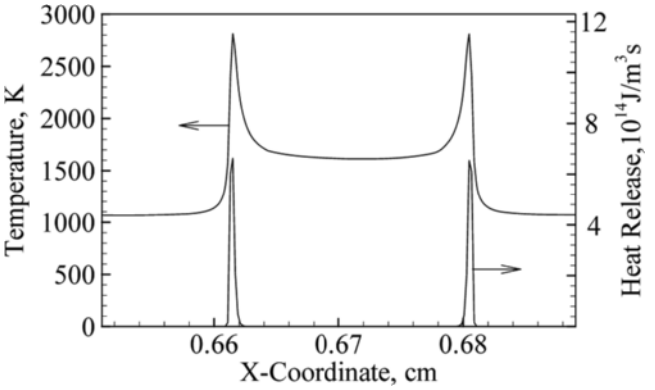

Figure 14 Temperature and heat-release distributions at 1 μm above propellant surface ($p = 100$ atm, AP/HTPB: 70/30 and $d_{AP} = 200$ μm).

An increase in *Da* would move the flame closer to the propellant surface and enhance the diffusion flame strength (Jackson and Buckmaster, 2000). Also, a decrease in *Pe* would lead to a larger amount of diffusive mixing, giving rise to a thicker flame zone. The characteristic reaction and diffusion time scales at a chamber pressure of 100 atm are estimated to be 10^{-7}–10^{-8}s and 10^{-5}s, respectively, leading to a high Damköhler number, *Da*, in the range of 100–1000. In an effort to extend this discussion, an extensive analysis is carried out to explore the effect of mass diffusion, flow convection, and reaction rate on the flame structure.

Effects of Reaction Rate

In the present study, on account of the high temperatures of the reactants (~900 K for the fuel stream and ~1400 K for the oxidizer stream), chemical reactions are initiated soon after the fuel and oxidizer are in contact. The maximum heat release takes place at about 1 μm above the propellant surface and serves as a flame

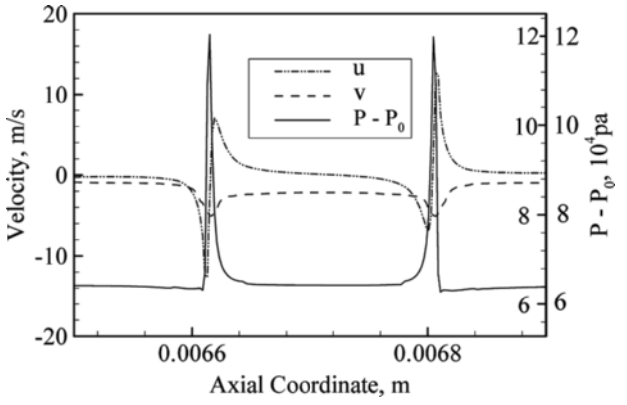

Figure 15 Velocity and pressure distributions at 1 μm above propellant surface ($p = 100$ atm, AP/HTPB: 70/30 and $d_{AP} = 200$ μm).

holder for the entire diffusion flame, as shown in Figures 11 and 14. The flame structure is similar to the CH_4/O_2 flame described by Prasad and Price (1992). In their work, fuel and oxidizer are released from the surface at the room temperature and pressure. There exists a region close to the initial contact point of the fuel and oxidizer streams where the temperature is lower than the mixture ignition temperature. The chemical reaction rate in this region is very slow, but the inter-diffusion between fuel and oxidizer is much faster (low Damköhler number), allowing a nearly premixed flow. The temperature of the premixed mixture continuously increases as it approaches the diffusion flame. As the ignition temperature is reached, the chemical reaction occurs along with a rapid heat release. The partially premixed flame so formed is referred to as the leading edge flame (LEF). The location of the LEF is about 1000 μm above the injection surface. This indicates that the time scales of the chemical reaction and diffusion play an important role in determining the flame-initializing location. In order to further elucidate this phenomenon, a numerical experiment is conducted. The pre-exponential factor in the reaction-rate expression for (R3) is artificially reduced to 1/100 of the original value, so that the reaction time scale is increased by 100 times and becomes comparable to the diffusion time scale. Consequently, the Damköhler number Da is in the range of 1–10. Figure 16 shows that the heat-release rate near the propellant surface decreases substantially, and the location corresponding to the peak value moves farther away from the surface. The diffusion flame is lifted about 21 μm above the propellant surface. Since the reaction and diffusion time scales are of the same order, there is sufficient time to enhance the species diffusion.

Unlike the flame-sheet model with an infinitely fast reaction rate ($Da \to \infty$), reactions take place in a much thicker region. If the reaction rate is further reduced, a premixed flame is expected to occur away from the propellant surface to initiate the final diffusion flame. This shows that the existence of the LEF is largely dependent on the reaction rate, and hence on the Damköhler number. In a practical rocket motor, since AP and HTPB decomposition products are released at very high temperatures and pressure, the final diffusion flame appears instantly when the fuel and

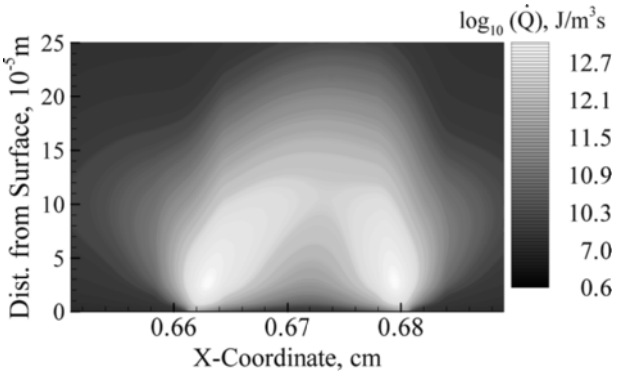

Figure 16 Distribution of heat release when the reaction rate is reduced to 1/100 of the original value ($p = 100$ atm, AP/HTPB: 70/30 and $d_{AP} = 200$ μm).

oxidizer come in contact with each other. Thus there exists a very bleak chance for diffusive mixing before the ignition takes place.

Effects of AP Particle Size and Pressure

The effect of AP particle size on the combustion of an AP/HTPB composite propellant is studied. Two different oxidizer segments, 200 and 20 μm, are selected, and the size of the fuel segment is varied accordingly. As the AP particle size decreases to 20 μm, the diffusion of reactants is encouraged due to the reduced length scale. The consumption of the oxidizer is much faster and the combustion is completed within a much shorter radial distance, as shown in Figure 17. The flame height decreases to 8 μm, compared to 140, for $d = 200$ μm. Figure 18 shows the corresponding temperature and heat-release distributions at 1 μm above the propellant surface. The increased temperature gradient at the propellant surface enhances the heat feedback to the condensed phase, and consequently the burning rate. The result is consistent with the experimental observation that the propellant burning rate increases with smaller oxidizer particle size.

The influence of chamber pressure on the flame structure and burning behavior is also explored. The chamber pressure exercises its influence in two ways. First, the mass diffusivity varies with pressure as follows:

$$D \propto \frac{T^{1.75}}{p} \tag{18}$$

According to Eqs. (15) and (18), the diffusion time scale becomes

$$t_d \propto p \tag{19}$$

Since t_d and t_F are of the same order of magnitude with $Pe \sim \mathrm{O}(1)$, Eqs. (15) and (19) lead to

$$\delta_f \propto \frac{d^2 \dot{m}_{AP}}{D\rho} \propto \frac{d^2 \dot{m}_{AP}}{T^{0.75}} \tag{20}$$

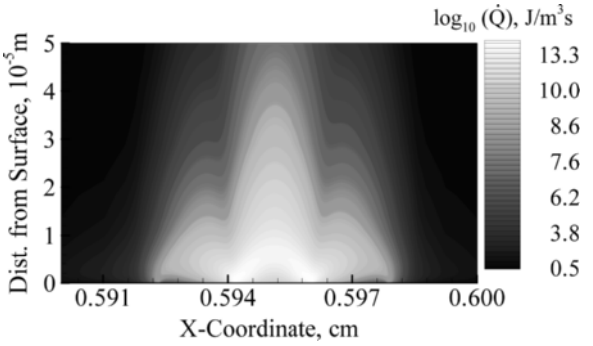

Figure 17 Distribution of heat-release rate ($p = 100$ atm, AP/HTPB: 70/30 and $d_{AP} = 20$ μm).

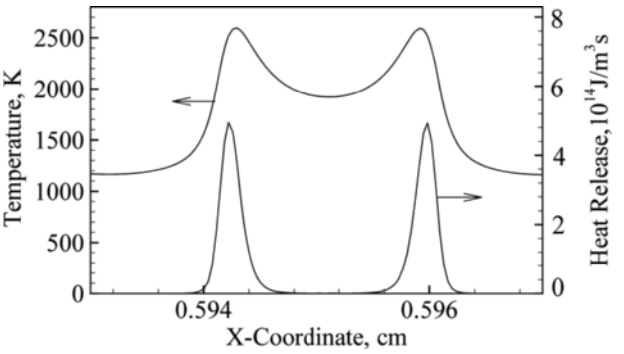

Figure 18 Temperature and heat-release distributions at 1 μm above propellant surface ($p = 100$ atm, AP/HTPB: 70/30 and $d_{AP} = 20$ μm).

The height of the final diffusion flame is directly proportional to the propellant mass flux $\dot{m}_{AP}$, which increases with pressure. Figure 19 shows the distribution of heat-release rate at 50 atm for $d = 200$ μm. Consistent with the above analysis, the flame height decreases to 76 μm, as compared to 140 μm at 100 atm. Second, at a given temperature, the reaction rate is related to the pressure as

$$\dot{\omega} \propto \rho^{1.75} \propto p^{1.75} \tag{21}$$

The associated time scale becomes,

$$t_c \equiv \rho/\dot{\omega} \propto p^{-0.75} \tag{22}$$

Figure 20 shows the heat release and temperature distributions near the propellant surface at 50 atm. In comparison with the case at 100 atm shown in Figure 14, both the temperature and heat release decreases with decreasing pressure, leading to a reduced propellant burning rate.

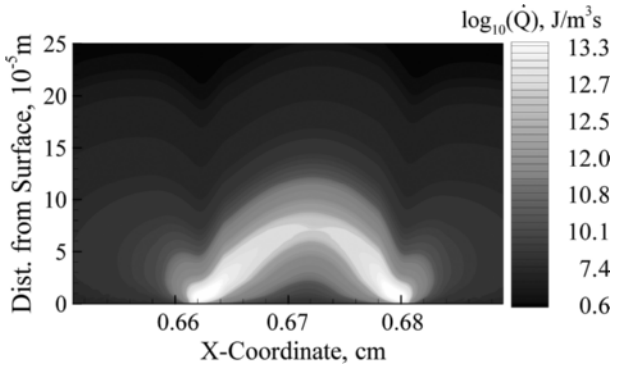

Figure 19 Distribution of heat-release rate ($p = 50$ atm, AP/HTPB: 70/30 and $d_{AP} = 200$ μm).

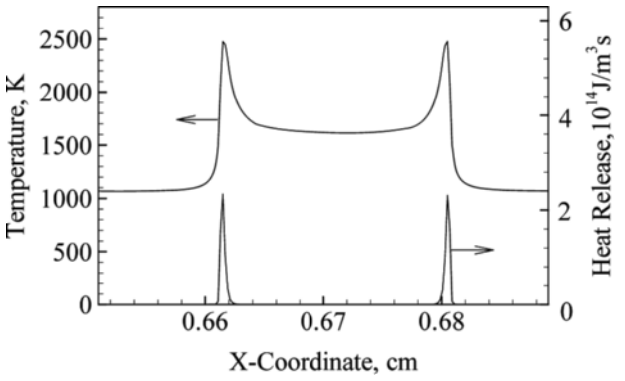

Figure 20 Temperature and heat-release distributions at 1 μm above propellant surface ($p = 50$ atm, AP/HTPB: 70/30 and $d_{AP} = 200$ μm).

Figure 21 shows a comparison of the calculated burning rate with the experimental data of Cohen et al. (1974). Reasonable agreement is obtained. The burning rate increases with an increase in the pressure and a decrease in the AP particle size. The over-prediction for the particle size of 20 μm may be attributed to the assumption that the AP and HTPB are thermally isolated in the condensed phase. If energy transfer is allowed between the two segments, the surface temperature of AP will be reduced, leading to a decrease in the overall burning rate. Another factor contributing to the discrepancy between the prediction and measurement is the neglect of the uneven regressions of AP and HTPB in the present analysis.

Effect of Cross Flow

The combustion of AP/HTPB composite propellant is influenced by the cross-flow in a motor. To investigate this effect, the location of the AP/HTPB sandwich is shifted downstream to 0.112 m from the head end, where the centerline velocity is

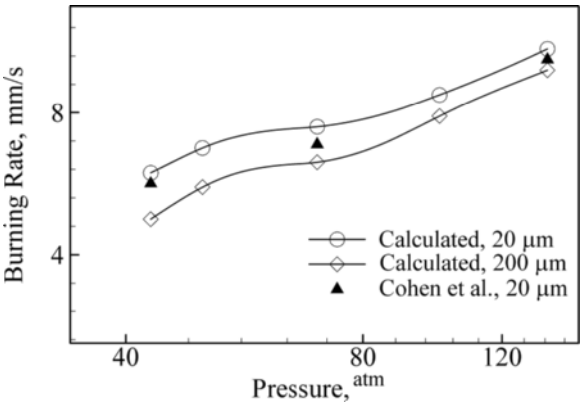

Figure 21 Effects of pressure and particle size on AP/HTPB propellant burning rate (AP/HTPB: 70/30).

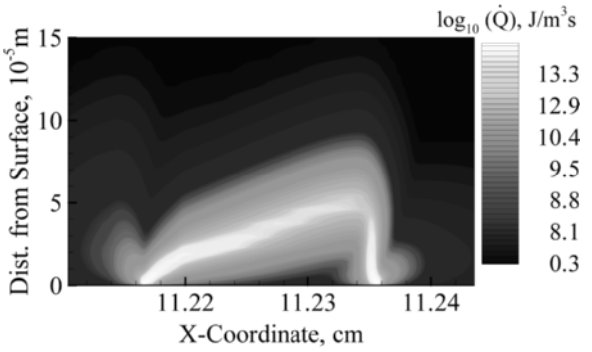

Figure 22 Distribution of heat release of propellant combustion at downstream location of x = 0.112 m ($p = 100$ atm, AP/HTPB: 70/30 and $d_{AP} = 200\,\mu$m).

93 m/s (Mach number ~ 0.1). Figure 22 shows the distribution of the heat-release rate at 100 atm for an AP segment width of 200 μm. As a consequence of the strong axial crossflow, the flame is tilted towards the propellant surface. The flame height decreases to a value of less than 50 μm, compared to 140 μm in the upstream region. The ensuing enhancement of the heat feedback from the flame zone to the condensed phase increases the propellant burning rate, a situation commonly referred to as erosive burning. A similar phenomenon of flame bending was observed by King (1978), based on an empirical approach.

Calculations were further performed to simulate the experiments of Saderholm (1964). The chamber length was increased to 0.3 m. Three different pressures of 20, 30, and 50 atm were considered. First the burning rates were calculated by placing the AP/HTPB segment near the head-end of the chamber to negate any erosive burning. Then the propellant segment was shifted to a downstream location, where the centerline velocity was 183 m/s (Mach 0.18). Figure 23 shows a comparison of the calculated and measured burning rates at different pressures with and without the presence of a crossflow.

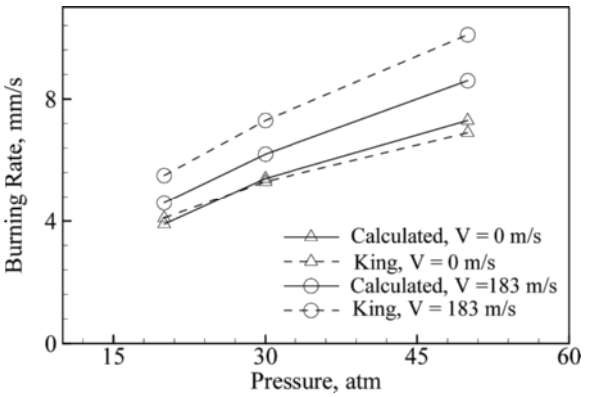

Figure 23 Effects of pressure and crossflow on AP/HTPB propellant burning rate (AP/HTPB: 73/27 and $d_{AP} = 20\,\mu$m).

Good agreement is achieved in the latter case. For the former case, the propellant burning rate is under predicted, which may be attributed to the lack of inclusion of the turbulence effects in the present study. Since the flow at the centerline has reached 183 m/s, transition to a turbulent flow is expected. King (1978) explained that the flame height was small enough to be in the viscous layer for wall-bounded shear flows. The argument, however, is debatable. Two factors should be taken into account in evaluating the effect of near-wall turbulence, viz., wall transpiration and combustion (Apte and Yang, 2002). Both play a role in enhancing the mixing due to turbulent eddies. The erosive burning thus results from the combined effects of flame bending and turbulence-enhanced mixing. As a next step, turbulent flowfields and turbulence-combustion interaction should be incorporated into the current model to predict the burning rates more accurately.

CONCLUSION

A theoretical/numerical model has been established for treating AP/HTPB composite-propellant combustion in a rocket-motor environment. The formulation takes into account the complete conservation equations in both the gas and condensed phases, and accommodates finite-rate chemical kinetics and variable thermophysical properties. A detailed parametric study was conducted on the gas-phase flame structures. The dependence of burning rate, flame stand-off distance, and spatial distribution of heat release on various factors (including chamber pressure, AP particle size, and gas-phase reaction rate) were studied in depth. A comparison between the time scales of chemical reaction and diffusion shows that the Damköhler number *Da* plays an important role in determining the flame-initializing location.

A lower value of *Da* favors the formation of partially premixed leading-edge flames (LEF). An increase in the pressure influences the combustion characteristics by modifying the mass diffusivities of the reactants and gas-phase reaction rates. A smaller size of AP particle leads to a shorter flame stand-off distance, and consequently increases the heat feedback to the condensed phase and the propellant burning rate. The phenomenon of flame bending towards the propellant surface has been observed under the influence of a crossflow. The under-estimation of the erosive burning rate in the present analysis, however, indicates the necessity for including the combined effect of flame bending and turbulence-enhanced mixing. Turbulent motion and turbulence-combustion interaction need to be incorporated into the current model to predict the burning rates more accurately.

NOMENCLATURE

A	pre-exponential factor
C_{AP}, C_{HTPB}	specific heat of AP and HTPB, respectively
d_{AP}	AP particle size
d_{HTPB}	HTPB binder size
h_i	specify enthalpy of species i
$h^0_{f,i}$	heat of formation of species i
$\dot{m}_{AP}$	mass burning rate of AP
$\dot{m}_{HTPB}$	mass burning rate of HTPB

p	pressure
Q	heat release
r_b	burning rate
T	temperature
T_s	surface temperature
t	time
u, v	velocity components in axial and radial coordinates, respectively
WM_i	molecular weight of species i
Y_i	mass fraction of species i

Greek Symbols

α	thermal diffusivity
λ	thermal conductivity
ρ	density
$\dot{\omega}_i$	mass rate of production of species i

Subscripts

c	condensed phase
g	gas phase
s	surface

REFERENCES

Apte, S. and Yang, V. (2001) Unsteady flow evolution in a porous chamber with surface mass injection, I: Free oscillation. *AIAA J.*, **39**, 1577–1586.

Apte, S. and Yang, V. (2002) Unsteady flow evolution and combustion dynamics of homogeneous solid propellant in a rocket motor. *Combust. Flame*, **131**, 110–131.

Arisawa, H. and Brill, T.B. (1996) Flash pyrolysis of hydroxyl-terminated polybutadiene (HTPB) II: Implications of the kinetics to combustion of organic polymers. *Combust. Flame*, **106**, 131–143.

Beck, W.H. (1987) Pyrolysis studies of polymeric materials used as binders in composite propellants: A review. *Combust. Flame*, **70**, 171–190.

Beckstead, M.W., Derr, R.L., and Price, C.F. (1970) A Model of composite solid-propellant combustion based on multiple flames. *AIAA J.*, **8**, 2200–2207.

Beddini, R.A. (1978) Reacting turbulent boundary-layer approach to solid propellant erosive burning. *AIAA J.*, **16**, 898–904.

Bilger, R.W., Jia, X., Li, J.D., and Nguyen, T.T. (1996) Theoretical and experimental study of composite solid propellant combustion. *Combust. Sci. Technol.*, **115**, 1–39.

Brill, T.B. and Budenz, B.T. (2000) Flash pyrolysis of ammonia perchlorate-hydroxyl-terminated-polybutadiene mixtures including selected additives. In Yang, V., Brill, T.B., and Ren, W.Z. (Eds.) *Solid Propellant Chemistry, Combustion and Motor Interior Ballistics, Progress in Astronautics and Aeronautics*, AIAA, NY, Vol. **185**, 3–23.

Buckmaster, J., Jackson, T.L., and Yao, J. (1999) An elementary discussion of propellant flame geometry. *Combust. Flame*, **117**, 541–552.

Cai, W. (2001) Two-phase Flow Interactions and Combustion of AP/HTPB Composite Propellant in Rocket Motors with Acoustic Oscillations, Ph.D. Dissertation, Pennsylvania State University, University Park, PA.

Chaiken, R.F. and Anderson, W.H. (1960) The role of binder in composite propellant combustion. *ARS Prog. Astro. Rocket*, **I**, 227–249.

Chen, J.K. and Brill, T.B. (1991) Chemistry and kinetics of hydroxyl-terminated polybutadiene (HTPB) and diisocyanate-HTPB polymers during slow decomposition and combustion-like conditions. *Combust. Flame*, **87**, 217–232.

Chorpening, B.T. and Brewster, M.Q. (2002) Combustion behavior of AP/HTPB propellant sandwiches with Peclet and Damköhler number variations. *Combust. Sci. Technol.*, **174**(4), 39–60.

Chu, W. and Yang, V. (1996) Combustion of AP-based composite propellant in a rocket motor flow environment. *32nd Joint Propulsion Conference, AIAA*, 96–2885.

Cohen, N.S., Fleming, R.W., and Derr, R.L. (1974) Role of binders in solid propellant combustion. *AIAA J.*, **12**, 212–218.

Glick, R.L. (1974) On statistical analysis of composite solid propellant combustion. *AIAA J.*, **12**, 384–385.

Godon, J.C., Duterque, J., and Lengelle, G. (1992) Solid propellant erosive burning. *J. Propul. Power*, **8**(4), 741–747.

Gordon, S. and McBride, B.J. (1994) Computer program for calculation of complex chemical equilibrium compositions and applications. *NASA Reference Publication 1311*.

Guirao, C. and Williams, F.A. (1971) A model for aluminum perchlorate deflagration between 20 and 100 atm. *AIAA J.*, **9**(7), 1345–1356.

Hegab, A., Jackson, T.L., Buckmaster, J., and Stewart, D.S. (2001) Nonsteady burning of periodic sandwich propellants with complete coupling between the solid and gas phases. *Combust. Flame*, **125**, 1055–1070.

Hermance, C.E. (1960) A model of composite propellant combustion including surface heterogeneity and heat generation. *AIAA J.*, **4**, 1629–1637.

Hsieh, S.Y. and Yang, V. (1997) A preconditioned flux-differencing scheme for chemically reacting flows at all Mach numbers. *Int. J. Comp. Fluid Dyn.*, **8**, 31–49.

Ibiricu, M.M. and Williams, F.A. (1975) Influence of externally applied thermal radiation on the burning rates of homogeneous solid propellants. *Combust. Flame*, **24**, 185–198.

Jackson, T.L. and Buckmaster, J. (2000) Nonpremixed periodic flames supported by heterogeneous propellants. *J. Propuls. Power*, **16**(3), 498–504.

Jackson, T.L. and Buckmaster, J. (2002) Heterogeneous propellant combustion. *AIAA J.*, **40**(6), 1122–1130.

Jacobs, P.W.M. and Whitehead, H.M. (1969) Decomposition and combustion of ammonium perchlorate. *Chem. Rev.*, **4**, 551–590.

Jia, X. and Bilger, R.W. (1994) The Burke-Schumann diffusion flame with zero net flux boundary conditions. *Combust. Sci. Technol.*, **99**, 371–376.

King, M.K. (1978) A model of erosive burning of composite propellants. *J. Spacecraft*, **15**(3), 139–146.

King, M.K. (1981) Experimental and theoretical study of the effects of pressure and crossflow velocity on composite propellant burning rate. *Proc. Combust. Instit.*, **18**, 207–215.

Kishore, K. (1979) Comprehensive view of the combustion models of composite solid propellants. *AIAA J.*, **17**, 1216–1224.

Knott, G.M. and Brewster, M.Q. (2000) Two-dimensional combustion modeling of heterogeneous solid propellants with finite Peclet number. *Combust. Flame*, **121**, 91–106.

Knott, G.M. and Brewster, M.Q. (2002) Modeling the combustion of propellant sandwiches. *Combust. Sci. Technol.*, **174**, 61–90.

Knott, G.M., Jackson, T.L., and Buckmaster, J. (2001) Random packing of heterogeneous propellants. *AIAA J.*, **39**(4), 678–686.

Lengelle, G. (1970) Thermal degradation kinetics and surface pyrolysis of vinyl polymers. *AIAA J.*, **8**(11), 1989–1998.

Massa, L., Jackson, T.L., and Buckmaster, J. (2005) New kinetics for a model of heterogeneous propellant combustion. *J. Propul. Power*, **21**(5), 914–924.

Nachbar, W. and Parks (1960) A Theoretical study of the burning of a solid propellant sandwich. *ARS Prog. Astronaut. Rocketry*, **I**, 207–226.

Oefelein, J.C. (1997) Simulation and Analysis of Turbulent Multiphase Combustion Processes at High Pressures. *Ph.D. Dissertation, Pennsylvania State University*.

Parr, T.P. and Hanson-Parr, D.M. (1996) Solid propellant diffusion flame structure. *Proc. Combust. Instit.*, **27**, 1981–1987.

Prasad, K. and Price, E. W. (1992) A numerical study of the leading edge of laminar diffusion flames. *Combust. Flame*, **90**, 155–173.

Price, E.W. (1995) Effect of multidimensional flamelets in composite propellant combustion. *J. Propul. Power*, **11**(4), 717–728.

Price, E.W., Sambamurthi, J.K., Sigman, R.K., and Panyam, R.R. (1986) Combustion of ammonium perchlorate-polymer sandwiches. *Combust. Flame*, **63**(3), 381–413.

Radhakrishnan, T.S. and Rama Rao, M. (1981) Thermal decomposition pf ploybutadienes by pyrolysis gas chromatography. *J. Polymer Sci.*, **19**(12), 3197–3208.

Ramakrishna, P.A., Paul, P.J., and Mukunda, H.S. (2002) Sandwich propellant combustion: Modeling and experimental comparison. *Proc. Combust. Instit.*, **29**, 2963–2973.

Ramohalli, K.N.R. (1984) Steady-State burning of composite propellants under zero cross-flow situation. In Kuo, K.K. and Summerfield M. (Eds.) *Fundamentals of Solid-Propellant Combustion, Progress in Astronautics and Aeronautics*. AIAA, New York.

Razdan, M. and Kuo, K.K. (1982) Turbulent flow analysis of erosive burning of cylindrical composite solid propellants. *AIAA J.*, **20**(1), 122–127.

Reid, R.C., Prausnitz, J.M., and Poling, B.E. (1987) *The Properties of Gases and Liquids*, 4th ed., McGraw-Hill, New York.

Renie, J.P. and Osborn, J.R. (1983) Erosive burning. *AIAA J.*, **21**(12), 1681–1689.

Roh, T.-S., Tseng, I.-S., and Yang, V. (1995) Effects of acoustic oscillations on flame dynamics of homogeneous propellants in rocket motors. *J. Propul. Power*, **11**(4), 640–650.

Saderholm, C.A. (1964) A Characterization of erosive burning for composite H-series propellants. *AIAA Solid Propellant Rocket Conference*, Palo Alto, CA.

Seleznev, V.A., Pokhil, P.F., Maltsev, V.M., and Bavykin, I.B. (1969) An optical method of measuring the burning surface temperature of condensed systems. *Combust. Flame*, **13**, 139–142.

Shuen, J.S., Liou, M.S., and Leer, B.V. (1990) Inviscid flux-splitting algorithms for real gases with non-equilibrium chemistry. *J. Comput. Phys.*, **90**, 371–395.

Summerfield, M., Sutherland, G.S., Webb, M.J., Taback, H.J., and Hall, K.P. (1960) The burning mechanism of ammonium perchlorate propellants. *ARS Progress in Astronautics and Rocketry*, **I**, 141–182.

Tseng, L.S. and Yang, V. (1994) Combustion of a double-base homogeneous propellant in a rocket motor. *Combust. Flame*, **96**, 325–342.

Waesche, R.H.W. and Wenograd, J. (1969) Calculation of solid propellant burning rate from condensed-phase decomposition kinetics. *AIAA Paper*, 69–145 .

Westbrook, C.D. and Dryer, F.L. (1981) Simplified reaction mechanisms for the oxidation of hydrocarbon fuels in flames. *Combust. Sci. Technol.*, **27**, 31–43.

Zong, N. and Yang, V. (2007) An efficient preconditioning scheme for general fluid mixtures using primitive pressure-temperature variables. *Int. J. Comp. Fluid Dyn.*, **21**(5–6), 217–230.